Clay Minerals, (2017) **52**, 51–65

Tetrahedral charge and Fe content in dioctahedral smectites

S. KAUFHOLD[1,*], J.W. STUCKI[2], N. FINCK[3], R. STEININGER[4], A. ZIMINA[5], R. DOHRMANN[1,6], K. UFER[1], M. PENTRÁK[2] AND L. PENTRÁKOVÁ[2]

[1] *BGR, Bundesanstalt für Geowissenschaften und Rohstoffe, Stilleweg 2, D-30655 Hannover, Germany*
[2] *Department of Natural Resources and Environmental Sciences, University of Illinois, Urbana, Illinois, USA*
[3] *Karlsruher Institut für Technologie, Institut für Nukleare Entsorgung, Hermann-von-Helmholtz-Platz 1, 76344 Eggenstein-Leopoldshafen, Germany*
[4] *Karlsruher Institut für Technologie, Institut für Synchrotronstrahlung ANKA, Hermann-von-Helmholtz-Platz 1, 76344 Eggenstein-Leopoldshafen, Germany*
[5] *Karlsruher Institut für Technologie, Institut für Katalyseforschung und-technologie, Hermann-von-Helmholtz-Platz 1, 76344 Eggenstein-Leopoldshafen, Germany*
[6] *LBEG, Landesamt für Bergbau, Energie und Geologie, Stilleweg 2, D-30655 Hannover, Germany*

(*Received 8 November 2015; revised 28 November 2016; Associate Editor: Helge Stanjek*)

ABSTRACT: Natural aluminosilicates can contain Fe in tetrahedral or octahedral coordination. Amongst smectites, tetrahedral iron is known to occur in Fe-rich nontronites but few indications exist for the presence of tetrahedral Fe in smectites of the montmorillonite–beidellite series. A set of 38 different bentonites showed a correlation of tetrahedral charge and Fe content in their smectites. All materials with large tetrahedral charge were rich in Fe. This could be explained by a general tendency of Fe to enter the tetrahedral sheet. To investigate this correlation, nine materials were selected and investigated by Mössbauer, UV-Vis, Fe *K* pre-edge and EXAFS spectroscopy with respect to tetrahedral Fe ($Fe^{[IV]}$). The latter two methods were at the detection limit but Mössbauer and UV-Vis spectroscopy provided consistent results indicating the significance of both methods in spite of some scatter caused by the overall small amount of tetrahedral Fe. The results indicate the absence of any relation between Fe content and tetrahedral Fe. Tetrahedral Fe can be present in Fe-poor smectites and absent in the case of Fe-rich materials. This means that Fe-rich montmorillonites have a larger tetrahedral charge which is not caused by $Fe^{[IV]}$ but by $Al^{[IV]}$. A possible explanation for this indirect relation is based on: the coordination of Al^{3+} in the weathering/smectite-forming solutions determines the coordination in the precipitates; and the $Al^{[IV/VI]}$ ratio increases with increasing pH. The correlation could thus be explained if the pH of weathering solutions generally was higher in Fe-rich parent smectite rocks than in more acidic smectite parent rocks. The relation between tetrahedral charge and Fe content can probably be explained by different geochemical contexts throughout the formation of smectites which affect the coordination of dissolved Al.

KEYWORDS: dioctahedral smectites, tetrahedral charge, Fe content, beidellite, tetrahedral Fe.

Amongst smectites, tetrahedral iron is known to occur in Fe-rich nontronites but few indications exist for the presence of tetrahedral Fe in smectites of the montmorillonite–beidellite series. The calculation of the structural formula of smectites is based on some

* E-mail: s.kaufhold@bgr.de
https://doi.org/10.1180/claymin.2017.052.1.03

assumptions (Köster, 1977; Kaufhold *et al.*, 2011a). One assumption is that structural Fe does not enter the tetrahedral sheet but occurs exclusively in the octahedral sheet with 6-fold coordination. Tetrahedral Fe ($Fe^{[IV]}$) is only expected to be present in nontronite. Manceau *et al.* (2000a,b) investigated four nontronite samples and found tetrahedral Fe in only one nontronite (14–20% of the Fe in tetrahedral coordination). Gates *et al.* (2002) investigated an additional 12 nontronite samples and two ferruginous smectites using X-ray absorption fine spectroscopy/X-ray absorption near edge spectroscopy (XAFS/XANES) (Fe_2O_3 ranged from 21 to 44 mass%). The comparison of tetrahedral Fe content with total Fe content led to the conclusion that tetrahedral Fe is unlikely to be present in smectites with <34 mass% Fe_2O_3. According to Decarreau & Petit (2014) $Fe^{[IV]}$ was not detectable below 1.5 atoms per formula unit (near infrared, NIR, X-ray diffraction, XRD, and calculations). Bishop *et al.* (1999), using different techniques (UV-Vis spectroscopy, Mössbauer spectroscopy and infrared (IR) spectroscopy), found $Fe^{[IV]}$ even in ferruginous smectites (SWa-1) and not just in nontronites.

These previous studies were focused on Fe-rich smectites and some suggested that the tetrahedral Fe depends on the total Fe content (at least no tetrahedral Fe is expected in Fe-poor smectites). This relation was not tested for smectites with low–moderate Fe contents. In contrast, the relation between tetrahedral charge and Fe content is well established (Weaver & Pollard, 1975; Badraoui & Bloom, 1990; Bujdák *et al.*, 2001; Ryan & Huertas, 2009; Kaufhold *et al.*, 2011b; Fig. 1). Both relations may be explained if Fe occupies tetrahedral sites. A nearly constant $Fe^{[IV/VI]}$ ratio, as suggested by Decarreau & Petit (2014), would increase both the tetrahedral charge and the tetrahedral Fe with increasing Fe content. Paquet (1970), however, suggested a coupled reaction where a large amount of octahedral Fe would require Al to enter the tetrahedral sites.

The present study investigates the relation between tetrahedral charge and Fe content and hence the possible occurrence of Fe in the tetrahedral sheet of common smectites. Nine samples with a range of tetrahedral charges (5–65%/CEC) and Fe_2O_3 contents (1–16 mass% Fe_2O_3) were selected (circles shown in Fig. 1).

The possible occurrence of Fe in the tetrahedral sheet not only affects the calculation of the structural formula, it may also affect the properties of bentonites used for various applications (*e.g.* sorption processes). Knowing the proportion of tetrahedral Fe is essential in order to identify relations between bentonite properties and performances.

Kaufhold *et al.* (2011b) determined that the full width at half maximum (FWHM) of XRD d_{001} reflections of Cu-trien–exchanged smectite appears closely related to both tetrahedral charge and Fe content. Generally, the FWHM is related to the degree of structural order. The structural order appears to be affected either by the Fe content or tetrahedral charge of the smectites. The understanding of the tetrahedral charge/Fe content relation is important, therefore. The aim of the present study was to investigate the role of tetrahedral iron ($Fe^{[IV]}$) with respect to the correlation of tetrahedral charge and total Fe content.

MATERIALS AND METHODS

Nine bentonites with a significant range of tetrahedral charge and Fe content were selected from the BGR (Bundesanstalt für Geowissenschaften und Rohstoffe, Federal Institute for Geosciences, Germany) sample set (X-ray fluorescence (XRF): Kaufhold & Dohrmann, 2008; pH: Kaufhold *et al.*, 2008; mineralogical composition: Ufer *et al.*, 2008; Kaufhold *et al.*, 2012; variable charge: Kaufhold & Dohrmann, 2013; cation exchange capacity (CEC) data: Dohrmann & Kaufhold, 2009; exchangeable cations: Dohrmann & Kaufhold, 2010). The mineralogical and chemical compositions of these samples (described in the studies above) are summarized in Tables 1 and 2. The samples were used as bulk materials for analysis. The difference in Fe content of the <0.2 μm fraction and of the bulk material is small and Mössbauer spectroscopy indicated the absence of Fe oxyhydroxides in all samples bar one (B10). Sample B16 from Bavaria contains illite/muscovite which could also contain some tetrahedral Fe. The 10 Å phases of the Bavarian bentonites, however, are known to contain well crystallized, detrital mica with a generally small Fe content.

The tetrahedral charge was determined by measuring the CEC (Cu-trien method; Meier & Kahr, 1999; Kaufhold & Dohrmann, 2003) before and after Li treatment (Hofmann & Klemen, 1950). 0.5 g of each bentonite sample (Na form was used because Li exchange is easier) was subjected to a 2 M LiCl solution (500 mL) resulting in a 1000-fold excess of Li over Na. After 24 h of shaking and centrifugation, another 500 mL of 2 M LiCl was added and again shaken for 24 h. The samples were centrifuged, dialysed, dried at 60°C, and ground using a mortar mill for homogenization (~5 min to avoid amorphization). The samples were then heated at 250°C for 4 h.

https://doi.org/10.1180/claymin.2017.052.1.03 Published online by Cambridge University Press

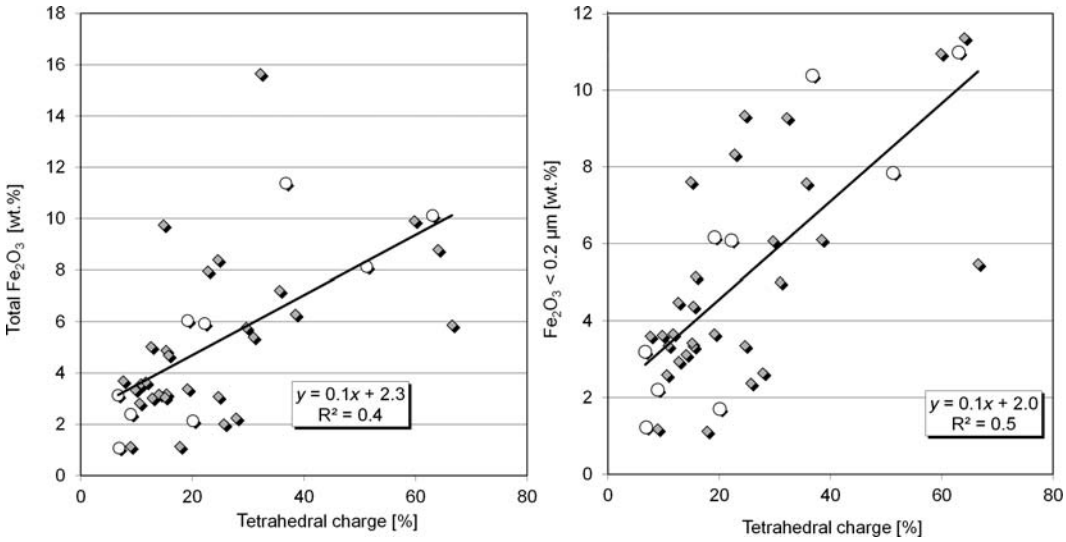

FIG. 1. Correlation of the amount of tetrahedral charge (determined with the Cu-trien method before and after Li-treatment) with total Fe_2O_3 (left) and Fe_2O_3 of the <0.2 µm fraction of 36 bentonites (B01–B38, without illite-smectite clays). Circles indicate selected samples; data were published by Kaufhold *et al.* (2011b).

These samples and precursor materials were investigated with respect to their CEC. The difference in the CEC before and after Li treatment/heating results from the ratio of octahedral and tetrahedral charge because at 250°C Li migrates into the structure to compensate the charge deficiency of the octahedral sheet (Hofmann & Klemen, 1950). The remaining charge after Li treatment, measured by CEC, is a result of tetrahedral charge only. Hence, the proportion of tetrahedral charge was determined by the difference in the CEC before and after the Hofmann & Klemen (1950) treatment. Notably, the Li treatment was conducted to determine the tetrahedral charge only. Samples studied with respect to tetrahedral Fe using other methods were not treated with Li.

The nine samples (ground to <20 µm) were analysed by variable-temperature (4–298 K) Mössbauer spectroscopy using a triangular-waveform, constant-acceleration spectrometer (Web Research, Inc., Edina, Minnesota, USA) equipped with a Janis Model SHI-850-5 closed-cycle cryostat (Janis Research, Inc., Wilmington, Massachusetts, USA) and a ^{57}Co gamma-ray source of initial activity of 50 mCi (suspended as 10 wt.% in a Rh foil). To reduce potential texture effects of the powdered samples, most samples were placed at an orientation of 54.7° relative to the axis of the gamma-ray beam. Spectra were fitted with doublets and sextets assuming Lorentzian line shapes using the *WinNormos* software package (WissEl [Wissenschaftliche Elektronik GmbH], Würmstraße 8, 82319 Starnberg, Germany). The velocity scale was calibrated from the spectrum of a 7 µm thick α-Fe(0) foil (iron in α-modification), assuming a magnetic hyperfine field (Bhf) for the Fe(0) to be 33.1 Tesla at 298 K and 33.9 Tesla at 77 and 4 K (Violet & Pipkorn, 1971). The isomer shift values for the samples, however, are reported here relative to the source rather than relative to this foil. The sample temperature during acquisition of the Mössbauer spectrum was that of liquid He (4 K), liquid N_2 (77 K), or room temperature (298 K).

Hyperfine parameters obtained from the Mössbauer fitted spectra were the isomer shift (δ), quadrupole splitting (Δ), and magnetic hyperfine field (Bhf). The calculation of hyperfine parameters was necessary in order to obtain relative peak areas for the various forms of Fe in the system. Calibration spectra revealed that vibrational interferences of the instrument were minimal, giving a line width for the Fe foil of ~0.27 mm/s with the cryostat in full operation. Spectra were acquired over the γ-ray energy range (measured in velocity) of ±11 mm/s or ±4 mm/s.

Spectra in the ultra-violet (UV) and visible (Vis) regions of the electromagnetic spectrum were obtained by diffuse reflectance using a Varian Cary 5 UV-Vis-NIR spectrophotometer in combination with an integrating sphere. Samples were mounted as dried

https://doi.org/10.1180/claymin.2017.052.1.03 Published online by Cambridge University Press

Table 1. Mineralogical composition, CEC data and tetrahedral charge of the selected samples (quantitative mineralogical composition based on Ufer *et al.*, 2008).

Sample		Smectite	Quartz	Illite / Muscovite	Kaolinite	Feldspar	Calcite	Dolomite	Chlorite	Cristobalite	Hem / Goethite	Ilmenite	Rutile / Anatase	Gypsum	Clinopt. / Heul.	Analcime	Pyrite	Fluorapatite	Na^+	K^+	Mg^{2+}	Ca^{2+}	sum cations	CEC	sum-CEC	tetrahedral charge
		[mass%]																	[meq/100 g]							[%/CEC]
B05	Milos	88	1			2	5						1	1			1		16	3	42	82	143	111	31	19
B08	Wyoming	67	17	2		8	2			1				1	1	1			71	0	1	15	87	66	21	7
B10	India	89	6				1				1	1	2						28	2	22	50	102	89	13	37
B13	Hungary	84	6		3	1	4						2					1	1	2	40	58	102	83	19	63
B16	Bavaria	70	7	19	3									1					0	2	25	54	81	65	16	22
B22	Argentina	76	4			8	0			12									70	1	3	30	105	95	10	7
B28	Indonesia	69	2			4				8					17				0	2	4	69	75	74	1	20
B36	Slovakia	75	11		2	8				3			0						0	2	17	36	54	56	−1	51
B37	Slovakia	63	11	9		8	7	1	0				0						1	1	27	56	84	85	−1	9

Table 2. Chemical composition of the nine selected bentonite bulk samples and Fe_2O_3 content of the <0.2 μm fraction.

Sample	SiO_2	TiO_2	Al_2O_3	Fe_2O_3	Fe_2O_3 (<0.2 μm)	MnO	MgO	CaO	Na_2O	K_2O	P_2O_5	SO_3	LOI	sum	C_{total}	C_{org}	C_{anor}	S_{total}
	[mass%]																	
B05	47.6	0.7	15.9	6.0	*6.2*	0.0	3.0	4.4	0.4	0.5	0.1	0.9	20.2	99.7	0.6	0.0	0.6	0.7
B08	66.8	0.1	15.7	3.1	*3.2*	0.0	1.5	0.9	2.6	0.4	0.0	0.2	8.3	99.7	0.2	0.0	0.2	0.1
B10	49.4	1.9	13.9	11.4	*10.4*	0.0	2.6	1.5	0.8	0.5	0.1	0.0	17.5	99.6	0.1	0.1	0.1	0.0
B13	44.6	2.0	16.2	10.1	*11.0*	0.1	2.1	3.1	0.1	0.6	0.3	0.0	20.4	99.6	0.5	0.1	0.5	0.0
B16	51.5	0.4	20.1	5.9	*6.1*	0.0	2.9	1.4	0.1	1.7	0.1	0.3	15.5	99.7	0.1	0.1	0.0	0.1
B22	62.4	0.2	15.0	1.1	*1.2*	0.0	3.3	1.0	2.3	0.4	0.1	0.0	13.9	99.8	0.0	0.0	0.0	0.0
B28	58.8	0.2	13.5	2.1	*1.7*	0.0	3.1	2.7	0.1	0.5	0.1	0.0	18.4	99.6	0.1	0.1	0.0	0.0
B36	61.7	0.8	17.5	8.1	*7.8*	0.1	1.6	1.3	0.4	1.4	0.1	<0.01	6.7	99.7	0.1	0.1	0.0	0.0
B37	63.3	0.1	20.1	2.4	*2.2*	0.1	3.4	1.9	0.5	0.8	0.0	0.1	7.0	99.6	0.3	0.2	0.1	0.2

LOI: loss on ignition, data from Kaufhold & Dohrmann (2008).

powders and referenced to a MgO white standard. Reflectance values were converted to absorbance using the Kubelka-Munk formula.

Information on the local chemical environment of Fe was obtained by probing the *K*-edge by X-ray absorption spectroscopy (XAS). All nine bentonites were prepared as pellets after dispersion in a binder. Fe *K*-edge XAS data were collected at the SUL-X beamline at ANKA (Karlsruhe, Germany) with a storage ring energy of 2.5 GeV and a ring current of 170–100 mA. The DCM (double crystal monochromator) was equipped with a pair of either Si(311) crystals to record pre-edge spectra or Si(111) crystals for EXAFS data collection (the Si(311) crystals have a better energy resolution than the Si(111) crystals). The energy was calibrated by assigning the first inflection of an iron foil measured along with all samples to 7112.0 eV. To reduce potential texture effects of the pellets, data were collected with an orientation of 35° relative to the electric field of the X-ray beam (at this 'magic' angle, any angular effect is extinguished). XANES spectra were collected for all samples, and four bentonites (B13, B16, B22, B36) were further selected for detailed Fe *K*-edge EXAFS study because of slightly different XANES results.

The Fe *K*-edge spectra have a weak pre-edge ~15 eV below the main edge that arises predominantly from the $1s \rightarrow 3d$ dipolar transition (Westre *et al.*, 1997; Manceau *et al.*, 2000a,b). However, 3*d* transitions are not allowed in O_h symmetry based on point group selection rules, and thus no pre-edge should be observed for octahedrally coordinated Fe. A very weak pre-edge feature, split into t_{2g}- and e_g-like components, is still observed experimentally and the intensity depends on local symmetry. The introduction of distortion at the Fe octahedral site allows part of the formerly forbidden transition. The pre-edge intensity of octahedrally coordinated Fe is also correlated with the Mössbauer quadrupole splitting (Waychunas *et al.*, 1983). In contrast, pre-edge features of 4-fold coordinated Fe have higher amplitude, which results from 3*d* and 4*p* orbital mixing in T_d symmetry (Wilke *et al.*, 2001). The pre-edge intensity can be used to evaluate the Fe coordination geometry. The pre-edges were modelled with pseudo-Voigt line shapes (Westre *et al.*, 1997) after subtraction of the background with an exponential function, following a procedure described by Finck *et al.* (2015). Fits of the pre-edges were provided by the software *OriginPro* 8.6 (function 'Peak Analyzer' in 'Peaks and Baselines').

Information on the local environment was obtained by data fitting of the EXAFS results. The EXAFS data were analysed following standard procedures by using the Athena and Artemis interfaces to the *Ifeffit* software (Ravel & Newville, 2005). The EXAFS spectra ($\chi(k)$) were extracted from the raw data and Fourier transforms (FT) were obtained from the $k^3 \times \chi(k)$ functions (4.1–13.0 Å^{-1} range selected with a Kaiser-Bessel window). Data fit was performed in *R* space (1.3–3.6 Å range selected with a Kaiser-Bessel window) using phase and amplitude functions calculated using *feff* 8.4 (Ankudinov *et al.*, 1998). The amplitude reduction factor was set to 0.82. The initial structure used for modelling is that reported by Tsipursky & Drits (1984) and the fits were performed assuming Fe located in a dioctahedral structure at octahedral position because the pre-edge data showed no evidence for tetrahedral Fe. Hence, $Fe^{[VI]}$ is coordinated to six oxygen atoms in the first ligand shell, and has three octahedral cationic next neighbours and four tetrahedral neighbours. Because Mg, Al and Si have very limited differences in backscattering amplitude, the model was simplified using only Al and Fe in the octahedral sheet and Si in the tetrahedral sheet. The proportions of Al and Fe in octahedral positions were allowed to vary during the fit but the sum was defined as being equal to 3. Two additional contributions were used: O atoms at ~3.7 Å and multiple scattering from O atoms at ~4 Å. The O atoms at ~3.4 Å were apparently not detected because of the corrugation of the oxygen basal plane. Typical uncertainties on EXAFS distances are ±0.02 Å and 20% on coordination numbers for well resolved atomic shells, and they increase for atomic shells located at larger interatomic distance. The fit quality was quantified by the R_f factor representing the absolute misfit between theory and data (the definition of this factor can be found in Vantelon *et al.* (2003) where it is referred to as the "*r* factor").

RESULTS

Mössbauer spectroscopy

The best Mössbauer spectrum for calculating tetrahedral Fe was the ±4 mm/s spectrum at either 4 or 77 K, although the other spectra were used to determine ancillary phases and structural Fe^{2+}. All spectra were fitted (red spectrum in Fig. 2) to extract the relative area of the tetrahedral Fe compound (Table 3). The largest percentages of the Mössbauer relative areas corresponding to tetrahedral Fe were found for samples B05 and B36. B22, a bentonite poor in Fe, showed the smallest value. However, the Mössbauer relative areas of the Fe-rich materials B10 and B13 were also relatively small.

https://doi.org/10.1180/claymin.2017.052.1.03 Published online by Cambridge University Press

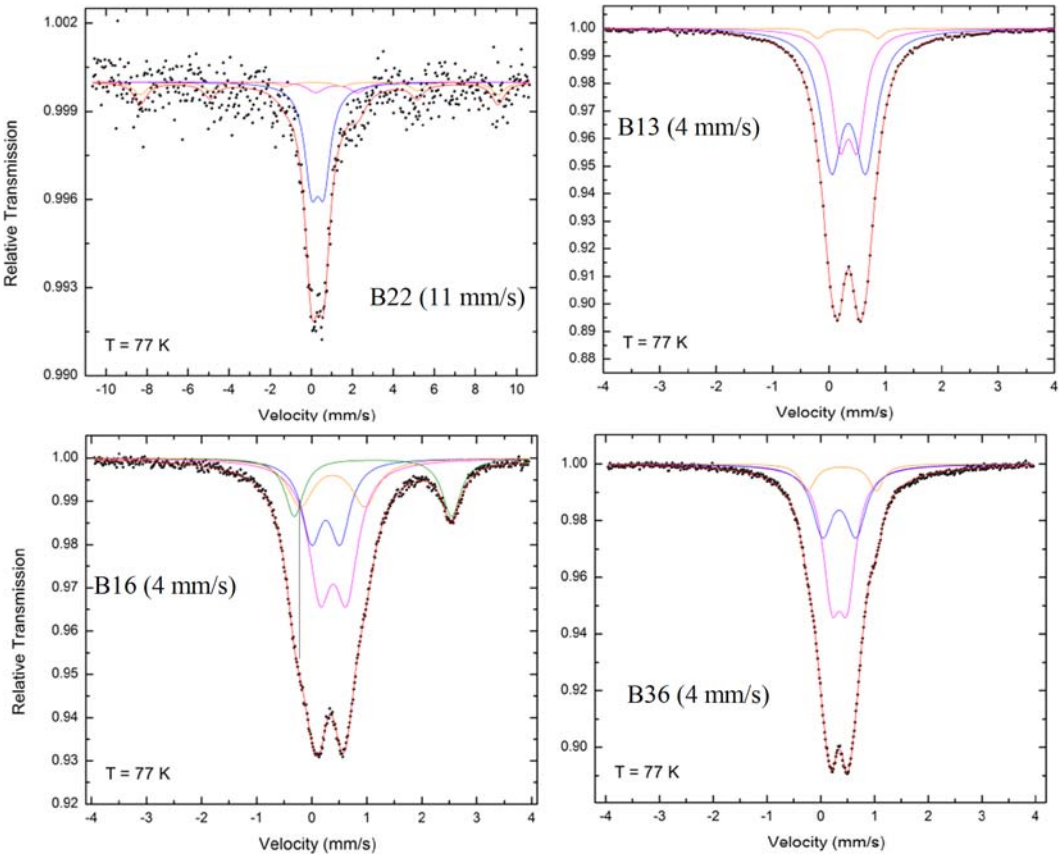

FIG. 2. Examples of Mössbauer spectra recorded at 77 K (samples B22, B13, B16, B36). Coloured lines represent the contributions used to deconvolute the spectrum.

UV-Vis spectroscopy

According to Merola & McGuire (2009) and Wu *et al.* (2004), UV-Vis spectroscopy can be used to determine the tetrahedral iron content. Based on a suitable baseline (*e.g.* linear from ~575–750 nm), the extinction at 650 nm can be obtained from the spectra and used for investigation of tetrahedral Fe. Three spectra covering the entire range of intensities as well as the extracted extinctions are shown (Fig. 3). The largest extinctions were found for samples B05 and B36 which is in accordance with Mössbauer results. The extinction at 650 nm of the Fe-rich sample B10 was difficult to determine because of the difficulty in finding a suitable background. Therefore, a range of extinctions was considered (0.000–0.100) representing different possible background corrections.

X-ray pre-edge spectroscopy

The pre-edge spectra of the nine samples are shown in Fig. 4. All pre-edges are of roughly similar intensity and split into two main features resulting from the crystal-field splitting in the octahedral environment: $O_h t_{2g}$ and $O_h e_g$. None of the sample showed compelling evidence for the presence of 4-fold coordinated Fe (*i.e.* Fe present in the tetrahedral sheet). The intensity increase for B05 above 7117 eV may be explained by the presence of pyrite (detected by XRD).

Despite the obvious similarity of the pre-edge peaks of all materials, small differences were observed (*e.g.* ratio of $O_h t_{2g}$ and $O_h e_g$ intensities). The spectra were fitted to extract quantitative information by using two components (Table 4). In all samples, the low height relative to the main edge (~0.02) and the energy

https://doi.org/10.1180/claymin.2017.052.1.03 Published online by Cambridge University Press

TABLE 3. Relative Mössbauer areas, Fe content and tetrahedral charge of the nine samples.

Sample	Fe minerals XRD/Mössbauer	Fe_2O_3 total [mass%]	Tet charge [%/CEC]	$Fe^{[IV]}$ relative Mössbauer area [%]
B05	1.5% pyrite	6.0	20	14.3
B08		3.1	7	10
B10	1% Goe/hem	11.4	37	3.7
B13		10.1	63	1.6
B16		5.9	22	9.3
B22		1.1	7	0
B28		2.1	20	4.7
B36		8.1	51	14.3
B37		2.4	9	5.5

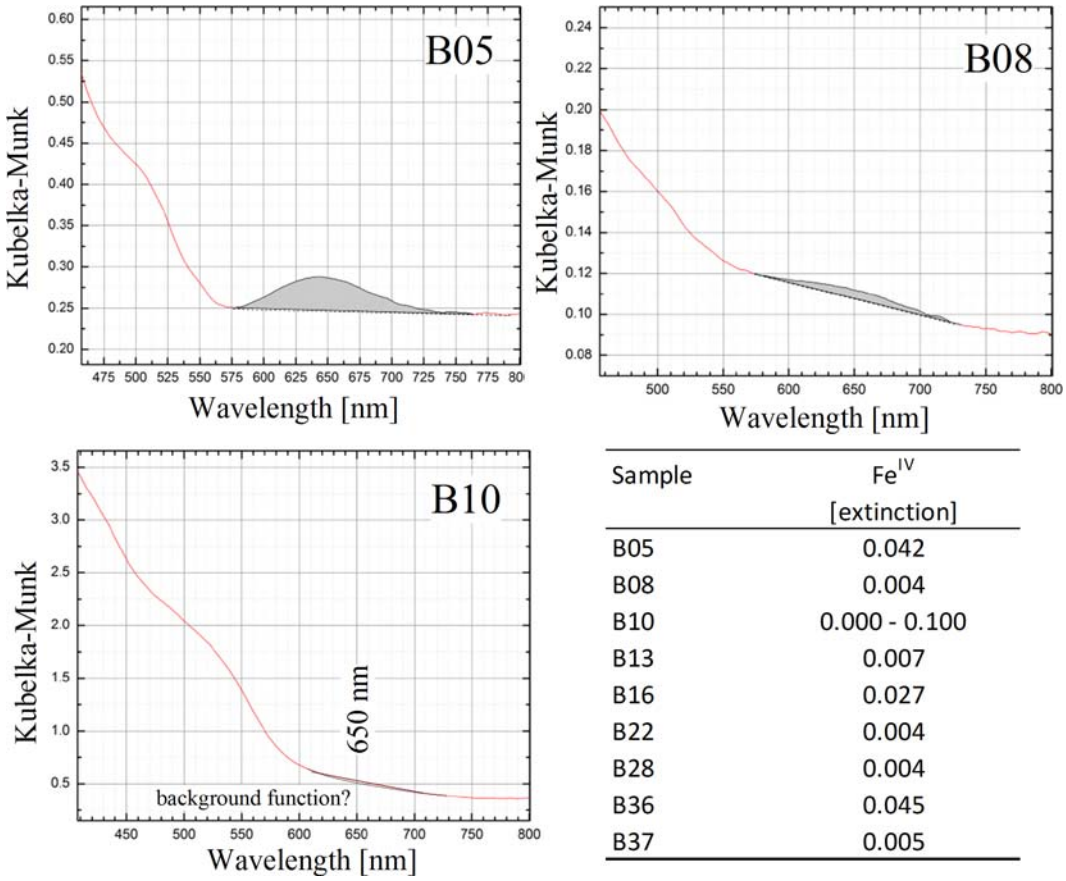

Sample	Fe^{IV} [extinction]
B05	0.042
B08	0.004
B10	0.000 - 0.100
B13	0.007
B16	0.027
B22	0.004
B28	0.004
B36	0.045
B37	0.005

FIG. 3. VIS spectra of three samples with different intensities at 650 nm.

separation around 1.5 eV are both consistent with octahedral Fe^{3+} (Westre *et al.*, 1997). Also, octahedral high-spin ferric complexes should show two features with an approximate intensity ratio of R = 3:2 (Westre *et al.*, 1997) and deviations from this ratio should reflect differences in covalency. There are large

https://doi.org/10.1180/claymin.2017.052.1.03 Published online by Cambridge University Press

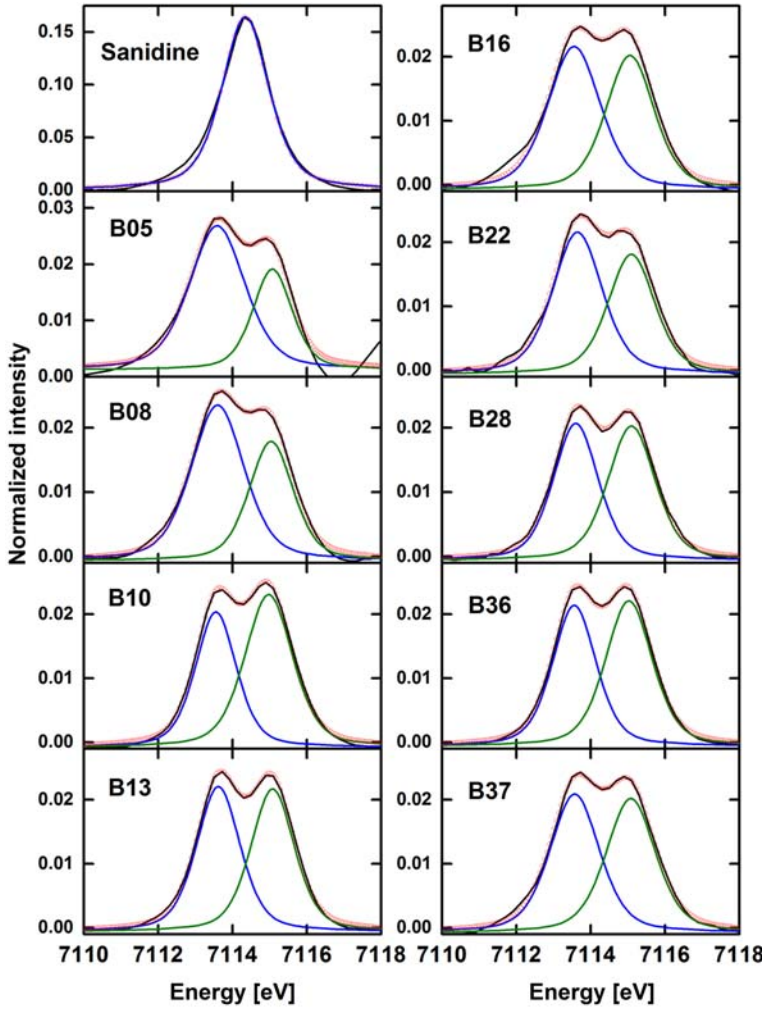

FIG. 4. Fe *K* pre-edge spectra of the nine bentonite samples with fits to the data. Also shown is the $Fe^{[IV]}$ reference sanidine for which the e- and t_2-like levels are close in energy und thus appear as a single peak (note the difference in scale between the tetrahedral and octahedral Fe). The fit results of the bentonites are presented in Table 4.

variations in R possibly related to differences in covalency and/or to the presence of (amorphous and crystalline) Fe-bearing impurities. For example, the value of R for structural Fe in the smectite, hectorite, has been reported to be significantly lower than for octahedral Fe in montmorillonite (Finck *et al.*, 2015), and it has been suggested that this difference may be attributed to the covalence because of fluorine substituting for OH groups in the Fe first coordination sphere in hectorite (greater electronegativity of F compared to OH groups). If there is an additional tetrahedral contribution, it may be weak. Notably, sanidine ($KAlSi_3O_8$) and hematite were tested as reference spectra for Fe in a tetrahedral and octahedral environment, respectively. However, the pre-edge features of the smectites are different and cannot be described as a mixture of these two phases.

EXAFS spectroscopy

The experimental EXAFS spectra of the four bentonites, together with the Fourier transforms (FTs) and the Fourier-filtered spectra, are shown in Fig. 5. In the experimental spectra, the features at $k \sim 5.3$ and

https://doi.org/10.1180/claymin.2017.052.1.03 Published online by Cambridge University Press

TABLE 4. Parameters used to fit the pre-edge spectra shown in Fig. 4.

	Component 1			Component 2				
	Position	Height	Area	Position	Height	Area	ΔE [eV]	R (area 1/2)
B05	7113.59	0.0256	0.0575	7115.08	0.0179	0.0284	1.49	2.02
B08	7113.60	0.0242	0.0519	7115.04	0.0185	0.0329	1.44	1.58
B10	7113.55	0.0212	0.035	7114.97	0.0239	0.0463	1.42	0.76
B13	7113.62	0.0227	0.0401	7115.08	0.0223	0.0394	1.46	1.02
B16	7113.56	0.0224	0.0478	7115.06	0.0210	0.0411	1.50	1.16
B22	7113.65	0.0222	0.0445	7115.10	0.0187	0.0355	1.45	1.25
B28	7113.60	0.0213	0.0389	7115.10	0.0209	0.0400	1.50	0.97
B36	7113.56	0.0221	0.0400	7115.03	0.0228	0.0433	1.47	0.92
B37	7113.57	0.0217	0.0435	7115.08	0.0210	0.0421	1.51	1.03

7.8 Å^{-1}, and to a lesser extent the feature at $k \approx$ 10.2 Å^{-1}, exhibit a significant trend that can be related to the Fe content. For example, the features at $k \approx 5.3$ and 7.8 Å^{-1} are shifted to higher wavenumbers with the Fe content. All FTs contain several peaks indicating the presence of different atomic shells. The FT peak at $R + \Delta R \approx 1.8$ Å is related to the first O shell and the contribution centred at ~3 Å originates from contributions of octahedral and tetrahedral neighbours as well as greater distances to O shells. Whereas the FT contribution from the first O shell is similar in all samples, the contribution centred at $R + \Delta R \approx 3$ Å exhibits significant differences. For example, two contributions can be seen in B22 at $R + \Delta R \approx 2.5$ and 3.0 Å, whereas only one contribution can be seen in the other samples, and this contribution is increasing in amplitude with Fe content. This finding hints clearly at different chemical environments.

The Fourier-transformed data were fitted (Table 5) to the structural model by fixing the coordination numbers equal to the theoretical values (sum of octahedral neighbours equal to three and four atoms in the tetrahedral sheet), the distances and the Debye-Waller term were allowed to vary. In all FTs, the first contribution could be well modelled considering six O atoms at $d_{Fe-O} = 2.01$–2.02 Å (Table 5). This Fe–O bond length is typical of Fe^{3+} cations in octahedral coordination (*e.g.* Manceau *et al.*, 2000a; Vantelon *et al.*, 2003); no tetrahedral contribution could be detected. According to the fit results, the observed differences in the next FT contribution(s) are due to the nature of octahedral neighbours only, the tetrahedral and greater-distance O back-scatterers being identical in all samples. No Fe-Fe pair could be detected in B22 whereas 1.3 Fe-Fe pairs were detected in B13 and B36. The larger number of octahedral Fe detected in these samples further correlates with the greater Fe content compared to B22 (Table 2). Additionally, the Al:Fe ratio based on the chemical composition is close to the ratio of neighbouring Al:Fe atoms detected, suggesting a random distribution within the octahedral sheet.

DISCUSSION

Comparison of the results

Mössbauer spectroscopy identified four samples (B05, B08, B16, B36) with significant $Fe^{[IV]}$; UV-Vis spectroscopy confirmed three of them (Fig. 6, Table 3). Sample B08 showed significant $Fe^{[IV]}$-related Mössbauer intensity but almost no UV-Vis extinction at 650 nm. Mössbauer and UV-Vis spectroscopy provided relative intensities – they were not yet calibrated against a material with known tetrahedral Fe content. Therefore, nontronite NG-1 with 17% tetrahedral Fe (Manceau *et al.*, 2000a) was used as reference to determine the percentage of tetrahedral iron (referred to as total iron rather than the amount of tetrahedral charge). Both the Mössbauer relative area (corresponding to $Fe^{[IV]}$) and the values obtained after calibration were compared with the UV-Vis data (Fig. 6).

The results of both methods show reasonable agreement which indicated the presence of tetrahedral Fe in Fe-poor smectites. The reason for the deviation of sample B08 cannot yet be explained. Three samples, B05 (Milos, Greece), B16 (Bavaria, Germany) and B36 (Slovakia) accommodate ~10% of their Fe in the tetrahedral sheet. The Fe content of the <0.2 μm

https://doi.org/10.1180/claymin.2017.052.1.03 Published online by Cambridge University Press

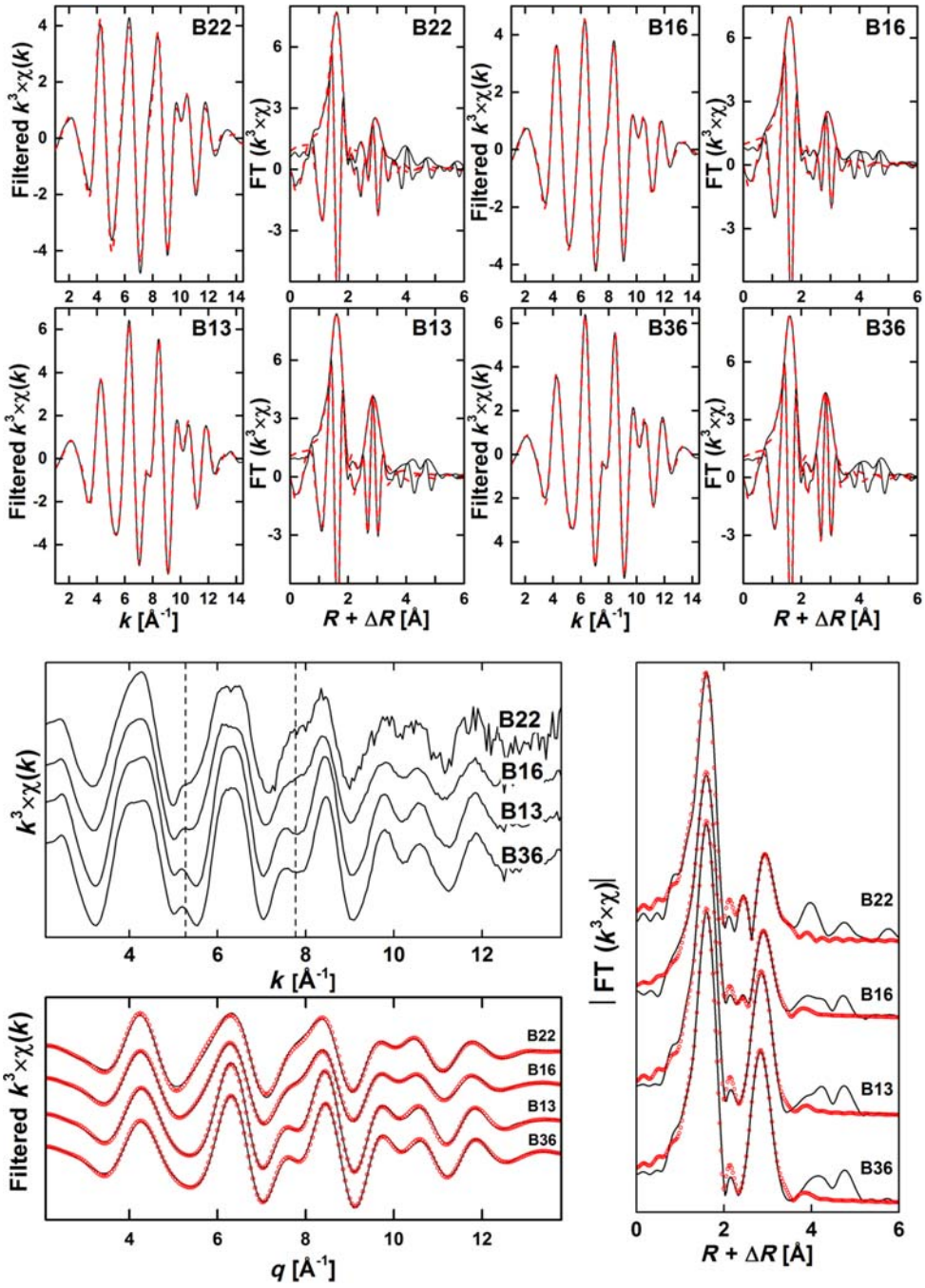

FIG. 5. Experimental (solid black lines) and modelled (dotted red line) EXAFS spectra with the corresponding Fourier transforms of the four samples. The vertical dashed lines highlight the difference in spectral features originating from the presence (or absence) of neighbouring Fe detected.

https://doi.org/10.1180/claymin.2017.052.1.03 Published online by Cambridge University Press

TABLE 5. Results from EXAFS data fitting.

	O1			Al1			Fe1			Si1			O2			O-O1			
Sample	*N*	*d*	σ^2	*N*	*d*	σ^2	*N*	*d*	σ^2	*N*	*d*	$\sigma\sigma^2$	*N*	*d*	σ^2	*N*	*d*	σ^2	R_f
B22	6	2.01	0.007	3	3.05	0.008	0			4	3.25	0.006	6	3.76	0.007	6	4.08	0.007	9.5
B16	6	2.02	0.008	2.2	3.06	0.004	0.8	3.06	0.003	4	3.29	0.008	6	3.72	0.010	6	4.00	0.007	2.3
B13	6	2.01	0.006	1.7	3.05	0.006	1.3	3.09	0.008	4	3.30	0.008	6	3.73	0.009	6	3.99	0.008	2.9
B36	6	2.01	0.006	1.7	3.04	0.004	1.3	3.06	0.004	4	3.30	0.004	6	3.71	0.009	6	3.98	0.008	3.3

N = coordination number, *d* = interatomic distance in Å, σ^2 = mean squared displacement or Debye Waller term in Å^2, R_f = quantifies the fit quality ($\Delta \times 10^3$).

fraction of these samples ranged from 4 to 5 mass% (6–8 mass% Fe_2O_3, given in mmol/g in Table 6). In conclusion, ~0.5% Fe is in tetrahedral coordination. These values/results were compared with both the pre-edge and XAFS data to try to identify systematic trends which could provide further information. Pre-edge and XAFS results were similar for all samples which indicated that both methods could not detect tetrahedral iron as a small fraction of the total iron. The fitted data were compared, therefore, with the Mössbauer data (Fig. 7).

The height and area parameters used for fitting the pre-edge spectra are strongly correlated and need not be considered separately, therefore. The best correlation of the Mössbauer and $Fe^{[IV]}$ values derived from UV-Vis data with the pre-edge fitting parameters is shown (Fig. 7a). This trend, however, is too weak for further interpretation. The height, at least of the second fitting component, depends on the Fe content (Fig. 7c). In conclusion, the pre-edge spectra do not resolve any difference in $Fe^{[IV]}$ in the nine samples. The parameters extracted from the EXAFS spectra, on the other hand, show good correlation with the Mössbauer- and UV-Vis-derived $Fe^{[IV]}$ values (Fig. 8).

Sigma square (Fig. 8a) is a mean squared displacement (Debye-Waller term) accounting for thermal and structural disorder. All data were collected at room temperature so that the variation reflects the difference in statistical distribution of interatomic distances. This may be attributed to substitution of Al for Fe where the size mismatch induces distortion.

The EXAFS wave amplitude of the backscattering atom increases with the atomic number (Manceau *et al.*, 2000a). Heavy elements are thus more easily detected than light elements, and this is especially true for distant neighbours as the wave amplitude decreases with $1/R^2$. This can be seen easily by comparing the EXAFS data of samples containing various amount of Fe (B16, B13, B36) and corroborates previous findings (*e.g.* Manceau *et al.*, 2000a; Vantelon *et al.*, 2003). For B22, no Fe back-scatterer was detected and separate $Al^{[VI]}$ and $Si^{[IV]}$ contributions are clearly distinguished (two peaks in the 2.5–3.5 Å range). In contrast, only one single FT peak centred at 2.8–3.0 Å was observed in all other samples where $Fe^{[VI]}$ was detected. For Fe located at octahedral sites, $Fe^{[VI]}$–$Al^{[VI]}$ and $Fe^{[VI]}$–$Fe^{[VI]}$ have similar distances but their EXAFS contributions are out of phase because of the π phase shift between Fe and Al back-scatterers. In contrast, the $Fe^{[VI]}$ and $Si^{[IV]}$ contributions are not out of phase because of differences in the bond lengths. However, the Si contribution is overwhelmed by that of $Fe^{[VI]}$

https://doi.org/10.1180/claymin.2017.052.1.03 Published online by Cambridge University Press

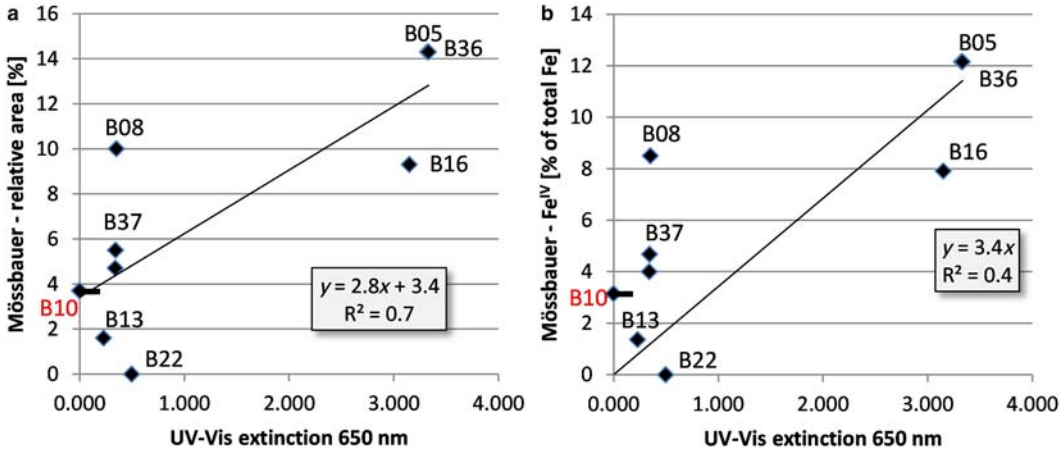

FIG. 6. Comparison of the UV-Vis extinction at 650 nm with the (a) Mössbauer relative area (of the tetrahedral Fe contribution) and (b) amount of tetrahedral Fe obtained after calibration of Mössbauer spectra with NG-1 and fixing the regression at the origin.

TABLE 6. Summary of the final data for the tetrahedral charge and $Fe^{[IV]}$ of the samples.

Sample	Fe_2O_3 total [mass%]	Fe <0.2 µm [mmol/g]	Tet charge [%/CEC]	$Fe^{[IV]}$ relative Mössbauer area [%]	$Fe^{[IV]}$ Mössbauer calibration [%/total Fe]	UV 650 nm [extinction]
B05	6.0	0.8	20	14	12	3.3
B08	3.1	0.4	7	10	9	0.4
B10	11.4	1.3	37	4	3	0.0–0.1
B13	10.1	1.4	63	2	1	0.2
B16	5.9	0.8	22	9	8	3.1
B22	1.1	0.2	7	0	0	0.5
B28	2.1	0.2	20	5	4	0.3
B36	8.1	1.0	51	14	12	3.3
B37	2.4	0.3	9	6	5	0.3

0 = below detection limit

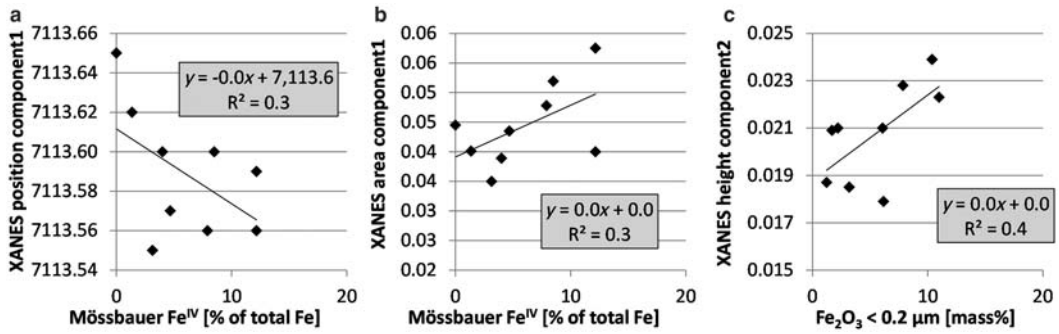

FIG. 7. Correlation of selected parameters used to fit the pre-edge spectra.

https://doi.org/10.1180/claymin.2017.052.1.03 Published online by Cambridge University Press

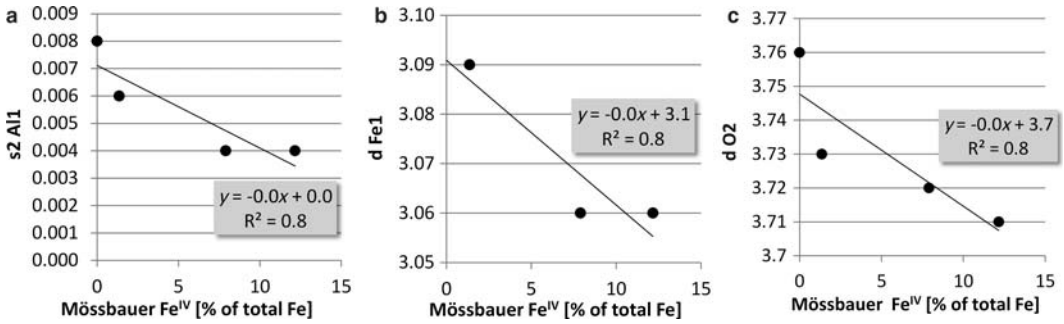

FIG. 8. Correlation of selected parameters used to fit the XAFS spectra.

because of greater Fe scattering intensity, and, with increasing amount of Fe detected, the intensity of the FT peak (sum of octahedral and tetrahedral neighbours) increases.

During the fit, the sum $Al^{[VI]} + Fe^{[VI]}$ was kept equal to 3.0. If Fe was needed to fit the data, the Al content was reduced accordingly. Al without any other fitting parameter cannot account for the intensity of the peak originating from octahedral and tetrahedral neighbours so that $Fe^{[VI]}$ (more intense EXAFS amplitude) had to be used to fit the data. The relation between Fe content and *b* cell-edge length of the smectite is well established (*e.g.* Heuser *et al.*, 2013). As the Fe content increases, the cell parameter increases and thus the interatomic distances (Fe–Fe, Fe–O2) increase also. The correlations shown in Fig. 8b,c, therefore, can be explained by the Fe content and not by tetrahedral Fe. Overall, no direct evidence for $Fe^{[IV]}$ was found by XAS because the amount of tetrahedral Fe was too small. All data are summarized (Table 6).

Comparison of the tetrahedral iron with tetrahedral charge

The aim of the present study was to investigate the role of tetrahedral iron ($Fe^{[IV]}$) with respect to the correlation of tetrahedral charge and Fe content. Therefore, the Fe content and tetrahedral charge were compared with the fraction of tetrahedral Fe derived from Mössbauer spectroscopy (Fig. 9). No correlation was observed, indicating that the tetrahedral Fe and tetrahedral charge are independent. As an example, the Fe-rich smectites of sample B13 which could be considered a beidellite rather than a montmorillonite (>60% tetrahedral charge) does not contain any tetrahedral Fe. Neither Mössbauer nor UV-Vis spectroscopy showed any signal indicating even a few percent tetrahedral Fe. On the other hand, Fe-rich bentonites with tetrahedral Fe also exist (*e.g.* B36). Gates *et al.* (2002) did not expect tetrahedral Fe to be present in smectites (nontronites) with <34 mass% Fe_2O_3. The

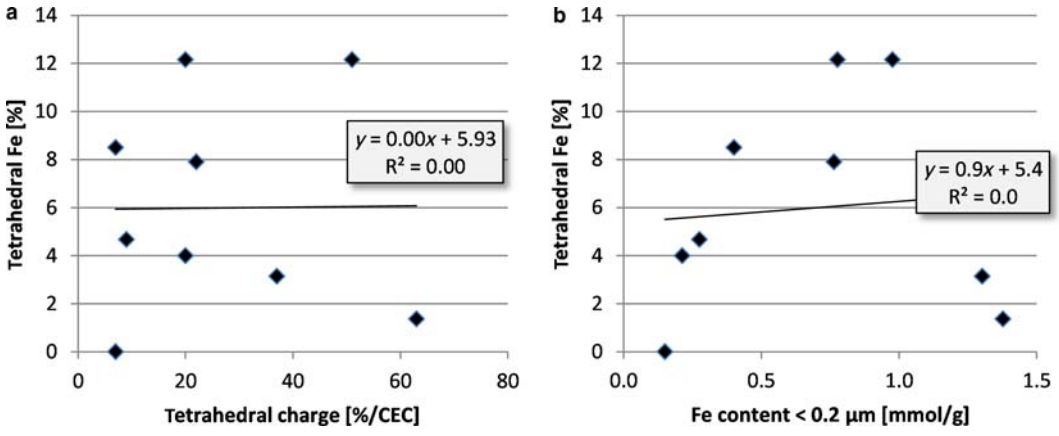

FIG. 9. Comparison of tetrahedral charge and Fe content (of the <0.2 µm fraction) with the proportion of tetrahedral Fe.

https://doi.org/10.1180/claymin.2017.052.1.03 Published online by Cambridge University Press

present study suggests tentatively that: (1) tetrahedral Fe is not related to the Fe content; and (2) smectites of bentonites with much less than 34 mass% Fe_2O_3 can contain up to 10% of their Fe in tetrahedral coordination.

To calculate the percentage of $Fe^{[IV]}$ relative to the total charge, the Fe_2O_3 content of the <0.2 μm fraction was converted to mmol/g and multiplied by the percentage of tetrahedral Fe/total Fe. Assuming a permanent charge of ~1 mmol/g results in 0–10% tetrahedral iron/permanent charge.

Reasons for the relation between Fe content and tetrahedral charge

A relation between tetrahedral Fe and total Fe content may be an explanation for the correlation between tetrahedral charge and total Fe content. A coupled mechanism or an indirect effect of Fe on the tetrahedral charge must be assumed. A small portion of the tetrahedral charge, however, can result from $Fe^{[IV]}$ but most of it results from $Al^{[IV]}$. In other words, large Fe contents in smectites force Al to enter the tetrahedral sheet.

Several possibilities could be discussed which would explain this relation (increased structure tension of Fe-rich smectites; Si deficiency throughout smectite formation from basaltic rocks). However, the most likely explanation is the dependence of the coordination of Al^{3+} on the pH. According to de Kimpe *et al.* (1961) the proportion of $Al^{[IV]}$ increases with increasing pH. Hence the correlation could be explained by generally greater pH values throughout weathering/smectitization of Fe-rich parent rocks compared to Si/Al-rich rocks. As reported by Gislason *et al.* (1996), the pH of water issuing from basaltic rocks may reach pH 10.

SUMMARY AND CONCLUSIONS

The aim of the present study was to determine the amount of tetrahedral Fe which could explain the correlation between tetrahedral charge and Fe content of dioctahedral smectites. Nine samples were selected with varying Fe contents and tetrahedral charge. They were investigated by Mössbauer spectroscopy (focusing on the relevant range), UV-Vis spectroscopy, Fe *K* pre-edge, and XAFS. Mössbauer and UV-Vis spectroscopy were in good agreement but the small amount of tetrahedral Fe in the samples was below the detection limit of pre-edge spectroscopy. Fourier-transformed XAFS spectra, however, indicated the significance of the Mössbauer and UV-Vis results. No correlation between tetrahedral charge and tetrahedral Fe was found. One Fe-rich smectite had up to 10% of its Fe in tetrahedral coordination and another Fe-rich bentonite did not contain any $Fe^{[IV]}$. In other words, dioctahedral smectites may contain up to 10% of their Fe in tetrahedral coordination which corresponds to ~10% of the permanent charge. Therefore, most of the tetrahedral charge results from $Al^{[IV]}$. Consequently a coupled mechanism has to be assumed to explain the relation of tetrahedral charge and Fe content. Aside from other options, the most likely explanation is the pH value which affects the coordination of Al^{3+} throughout smectitization. This explanation, however, is based on the assumption that weathering solutions penetrating basaltic rocks have higher pH values than those penetrating acidic rocks. The relation between pH of weathering solutions and Fe content of the parent rock, however, is not discussed further here.

REFERENCES

Ankudinov A.L., Ravel B., Rher J.J. & Conradson S.D. (1998) Real space multiple scattering calculation of XANES. *Physical Review B*, **58**, 7565–7576.

Badraoui M. & Bloom P.R. (1990) Iron-rich high-charge beidellite in Vertisols and Mollisols of the High Chaouia region of Morocco. *Soil Science Society of America Journal*, **54**, 267–274.

Bishop J.L., Murad E., Madejová J., Komadel P., Wagner U. & Scheinost A. (1999) Visible, Mössbauer and infrared spectroscopy of dioctahedral smectites: Structural analyses of the Fe-bearing smectites Sampor, SWy-1 and SWa-1. *11th International Clay Conference*, June, 1997, Ottawa, 413–419.

Bujdák J., Janek M., Madejová J. & Komadel P. (2001) Methylene blue interactions with reduced-charge smectites. *Clays and Clay Minerals*, **49**, 244–254.

Decarreau A. & Petit S. (2014) Fe^{3+}/Al^{3+} partitioning between tetrahedral and octahedral sites in dioctahedral smectites. *Clay Minerals*, **49**, 657–665.

Dohrmann R. & Kaufhold S. (2009) Three new, quick CEC methods for determining the amounts of exchangeable calcium cations in calcareous clays. *Clays and Clay Minerals*, **57**, 338–352.

Dohrmann R. & Kaufhold S. (2010) Determination of exchangeable calcium of calcareous and gypsiferous bentonites. *Clays and Clay Minerals*, **58**, 79–88.

Finck N., Schlegel M.L. & Bauer A. (2015) Structural iron in dioctahedral and trioctahedral smectites: a polarized XAS study. *Physics and Chemistry of Minerals*, **42**, 847–859.

Gates W.P., Slade P.G., Lanson B. & Manceau A. (2002) Site occupancies by iron in nontronites. *Clays and Clay Minerals*, **50**, 223–239.

Gislason S.R., Arnorsson S. & Armannsson H. (1996) Chemical weathering of basalt in southwest Iceland:

https://doi.org/10.1180/claymin.2017.052.1.03 Published online by Cambridge University Press

Effects of runoff, age of rocks and vegetative/glacial cover. *American Journal of Science*, **296**, 837–907.

Heuser M., Andrieux P., Petit S. & Stanjek H. (2013) Iron-bearing smectites: A revised relationship between structural Fe, *b* cell edge lengths and refractive indices. *Clay Minerals*, **48**, 97–103.

Hofmann U. & Klemen R. (1950) Verlust der Austauschfähigkeit von Lithiumionen an Bentonit durch Erhitzung. *Zeitschrift für anorganische Chemie*, **262**, 95–99.

Kaufhold S. & Dohrmann R. (2003) Beyond the Methylene Blue method: determination of the smectite content using the Cu-trien method. *Zeitschrift für Angewandte Geologie*, **2**, 13–18.

Kaufhold S. & Dohrmann R. (2008) Detachment of colloidal particles from bentonites in water. *Applied Clay Science*, **39**, 50–59.

Kaufhold S. & Dohrmann R. (2013) The variable charge of dioctahedral clay minerals. *Journal of Colloid and Interface Science*, **390**, 225–233.

Kaufhold S., Dohrmann R., Koch D. & Houben G. (2008) The pH of aqueous bentonite suspensions. *Clays and Clay Minerals*, **56**, 338–343.

Kaufhold S., Dohrmann R., Stucki J. & Anastácio A.S. (2011a) Layer charge density of montmorillonite – closing the gap between structural formula method and alkyl ammonium method. *Clays and Clay Minerals*, **59**, 200–211.

Kaufhold S., Dohrmann R., Ufer K., Kleeberg R. & Stanjek H. (2011b) Cu trien exchange to improve the analytical understanding of smectites. *Clay Minerals*, **46**, 411–420.

Kaufhold S., Hein M., Dohrmann R. & Ufer K. (2012) Quantification of the mineralogical composition of clays using FTIR spectroscopy. *Journal of Vibrational Spectroscopy*, **59**, 29–39.

de Kimpe C., Gastuche M.C. & Brindley G.W. (1961) ionic coordination in alumino-silicic gels in relation to clay mineral formation. *American Mineralogist*, **46**, 1370–1381.

Köster H.M. (1977) Die Berechnung kristallchemischer Strukturformeln von 2:1-Schichtsilikaten unter Berücks ichtigung der gemessenen Zwischenschichtladungen und Kationenumtauschkapazitäten sowie die Dars tellung der Ladungsverteilung in der Struktur mittels Dreieckskoordinaten. *Clay Minerals*, **12**, 45–54.

Manceau A., Lanson B., Drits V.A., Chateigner D., Gates W.P., Wu J., Huo D. & Stucki J.W. (2000a) Oxidation-reduction mechanism of iron in dioctahedral smectites: I. Crystal chemistry of oxidized reference nontronites. *American Mineralogist*, **85**, 133–152.

Manceau A., Drits V.A., Lanson B., Chateigner D., Wu J., Huo D., Gates W.P. & Stucki J.W. (2000b) Oxidation-reduction mechanism of iron in dioctahedral smectites: II. Crystal chemistry of reduced Garfield nontronite. *American Mineralogist*, **85**, 153–172.

Meier L.P. & Kahr G. (1999) Determination of the cation exchange capacity (CEC) of clay minerals using the complexes of Copper (II) ion with triethylenetetramine and tetraethylenepentamine. *Clays and Clay Minerals*, **47**, 386–388.

Merola R.B. & McGuire M.M. (2009) Crystallographic site distribution and redox activity of Fe in nontronites determined by optical spectroscopy. *Clays and Clay Minerals*, **57**, 771–778.

Paquet H. (1970) Evolution géochimique des minéraux argileux dans les altérations et les sols des sédiments méditerrannéens et tropicaux à saisons contrastées. *Mémoire de la Service Carte Géologique Alsace Lorraine*, **30**, 212.

Ravel B. & Newville M. (2005) Athena, artemis, Hephaestus: data analysis for X-ray absorption spectroscopy using IFEFFIT. *Journal of Synchrotron Radiation*, **12**, 537–541.

Ryan P.C. & Huertas F.J. (2009) The temporal evolution of pedogenic Fe-smectite to Fe-kaolin via interstratified kaolin–smectite in a moist tropical soil chronosequence. *Geoderma*, **151**, 1–15.

Tsipursky S.I. & Drits V. (1984) The distribution of octahedral cations in the 2:1 layers of dioctahedral smectites studied by oblique-texture electron diffraction. *Clay Minerals*, **19**, 177–193.

Ufer K., Roth G., Kleeberg R., Stanjek H., Dohrmann R. & Bergmann J. (2004) Description of X-ray powder pattern of turbostratically disordered layer structures with a Rietveld compatible approach. *Zeitschrift für Kristallographie*, **219**, 519–527.

Vantelon D., Montarges-Pelletier E., Michot L.J., Briois V., Pelletier M. & Thomas F. (2003) Iron distribution in the octahedral sheet of dioctahedral smectites. An Fe K-edge X-ray absorption spectroscopy study. *Physics and Chemistry of Minerals*, **30**, 44–53.

Violet C.E. & Pipkorn D.N. (1971) Mössbauer Line Positions and Hyperfine Interactions in α Iron. *Journal of Applied Physics*, **42**, 4339–4342.

Waychunas G.A., Apted M.J. & Brown Jr, G.E. (1983) X-ray K-edge absorption spectra of Fe minerals and model compounds: near-edge structure. *Physics and Chemistry of Minerals*, **10**, 1–9.

Weaver C.E. & Pollard L.D. (1975) *The Chemistry of Clay Minerals*. Developments in Sedimentology, **15**, Elsevier, Amsterdam, 213 pp.

Westre T.E., Kennepohl P., DeWitt J.G., Hedman B., Hodgson K.O. & Solomon E.I. (1997) A multiplet analysis of Fe K-Edge 1s f 3d pre-edge features of iron complexes. *Journal of the American Chemical Society*, **119**, 6297–6314.

Wilke M., Farges F., Petit P.-E., Brown Jr G.E. & Martin F. (2001) Oxidation state and coordination of Fe in minerals: An Fe K-XANES spectroscopic study. *American Mineralogist*, **86**, 714–730.

Wu J., Xia Y. & Stucki J.W. (2004) Color temperature indicator. U.S. Patent No. 6,712,996.

https://doi.org/10.1180/claymin.2017.052.1.03 Published online by Cambridge University Press